Optics Letters

Vector plasmonic lattice solitons in nonlinear graphene-pair arrays

ZHOUQING WANG,[1] BING WANG,[1,*] KAI WANG,[1] HUA LONG,[1] AND PEIXIANG LU[1,2,3]

[1]Wuhan National Laboratory for Optoelectronics and School of Physics, Huazhong University of Science and Technology, Wuhan 430074, China
[2]Laboratory of Optical Information Technology, Wuhan Institute of Technology, Wuhan 430205, China
[3]e-mail: lupeixiang@hust.edu.cn
*Corresponding author: wangbing@hust.edu.cn

We investigate the vector plasmonic lattice solitons (PLSs) in nonlinear graphene-pair arrays (GPAs) consisting of periodically arranged double graphene sheets, which are spatially separated. There are two dispersion bands for the Bloch modes in the array due to the coupling of surface plasmon polaritons (SPPs) between the graphene pairs. The vector PLSs composed of two components originate from the nonlinear interaction of Bloch modes in different bands. Both components undergo mutual self-trapping through the balance between diffraction and self-focusing nonlinearity of graphene. Thanks to the strong confinement of SPPs, the vector PLSs can be squeezed into a lateral width of $\sim\lambda/100$. The study provides a promising approach to all-optical control on a deep-subwavelength scale. © 2016 Optical Society of America

Optical spatial solitons, the stationary propagation of a light beam with a constant transverse profile, are formed as the diffraction and nonlinear effects reach a balance in a nonlinear optical system [1,2]. As a special type of spatial soliton, vector solitons have attracted much attention for potential applications in developing light-control-light techniques [3–5]. The vector solitons have at least two mutually influenced components with both being conventional spatial solitons. Also, each component originates from an eigenmode of the considered optical system and is modulated by the nonlinear Kerr effect due to the strong electric field intensity of all components including itself. In order to ensure robust stationary propagation, the components of vector solitons are usually incoherent and are of different frequencies or different polarizations [3]. Recent progress has been made in spatial solitons by using dielectric and metallic waveguide arrays [6–11], where the light diffraction can be flexibly engineered [12]. Furthermore, the solitons in metallic waveguide arrays, namely, plasmonic lattice solitons (PLSs), possess significantly small lateral size, as they are formed by surface plasmon polaritons (SPPs), which are strongly concentrated on metal surfaces

[13,14]. The vector PLSs also have been demonstrated in metallic waveguide arrays and may find potential applications in subwavelength all-optical technology [9].

We have demonstrated that periodic graphene sheet arrays are able to play a similar role of metallic waveguide arrays in tailoring SPP diffraction [15,16]. However, the SPP mode in graphene is substantially different from that on metallic film. Apart from the common asymmetric SPP mode, there should be a long-range SPP mode on the metallic film, which corresponds to a plane wave in graphene. The difference is also applied for array structures. There are usually two dispersion bands corresponding to the propagating SPP Bloch modes in metallic waveguide arrays but only one nontrivial band in graphene sheet arrays. The other one refers to trivial plane waves due to the 2D feature of graphene. On the other side, SPPs on graphene exhibit stronger confinement, lower propagation loss, and flexible tunability in comparison with metals [17,18]. These features make graphene a competitive alternative to metals in manipulating SPPs.

In this work, we investigate the vector PLSs in nonlinear graphene-pair arrays (GPAs) considering that graphene is also an admirable nonlinear material [19–21]. Importantly, the structure is composed of periodical graphene pairs instead of single-layer graphene. A graphene pair consisting of two separated parallel graphene sheets can support symmetric and antisymmetric propagating SPP modes [22–24]. Consequently, there should be two dispersion bands for the GPAs. The vector PLSs are composed of two components belonging to different bands with different frequencies. The stationary propagation of vector PLSs is obtained by achieving the balance between the self-focusing nonlinearity of graphene and SPP diffraction. We also study the vector PLSs shaping by varying the chemical potential of graphene.

We start from investigating the linear properties of GPAs. As shown in Fig. 1, the structure is composed of alternative graphene sheets and the dielectric layers, which are arranged periodically along the x axis. The period of structure is $d = d_1 + d_2$ with d_1 representing the spacing of graphene in each period and d_2 the side-by-side distance of adjacent graphene pairs. The dielectric relative permittivity is denoted by ϵ_d. The surface conductivity $\sigma_g (\lambda, \mu_c, \tau)$ of graphene is governed
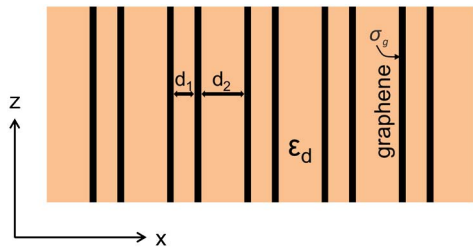
Fig. 1. Diagram of the GPA. The graphene pair in each period of the array is composed of double graphene sheets. The period of the GPA is given by $d = d_1 + d_2$.

by the Kubo formula [25], where λ is the incident wavelength in air, μ_c is the chemical potential of graphene, and τ is the momentum relaxation time. We consider the transverse magnetic (TM) waves propagating along the z direction. According to the Maxwell's equations and Bloch theorem, the dispersion relation of SPPs in GPAs reads as follows:

$$\cos(\varphi) = \cosh(\kappa d) + \zeta \sinh(\kappa d) + \frac{\zeta^2}{2} \sinh(\kappa d_1) \sinh(\kappa d_2), \tag{1}$$

where the Bloch momentum is given by $\varphi = k_x d$ with k_x the Bloch wave vector along the x direction, $\kappa = (k_z^2 - \epsilon_d k_0^2)^{1/2}$, $k_0 = 2\pi/\lambda$, k_z is the propagation constant, and $\zeta = i\kappa\eta_0\sigma_g/(\epsilon_d k_0)$ with η_0 the impedance in vacuum. The parameters are given by $d_1 = 60$ nm, $d_2 = 80$ nm, $\epsilon_d = 1$, $\mu_c = 0.15$ eV, and $\tau = 0.5$ ps [26,27].

The dispersion relation, the dependence of the propagation constant k_z on the lateral Bloch momentum, is shown in Fig. 2(a) for the wavelength $\lambda_1 = 9.8$ μm and $\lambda_2 = 10.2$ μm. In contrast with the metal-dielectric arrays [9], the bandgap is determined by the edge of the Brillouin zone for GPAs.
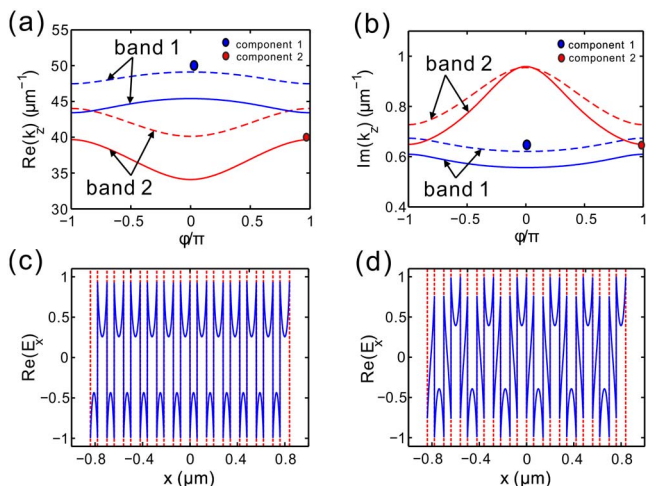
Fig. 2. (a) Real part of the propagation constants (k_z) of Bloch modes as a function of the Bloch momentum. Dash and solid curves correspond to $\lambda_1 = 9.8$ μm and $\lambda_2 = 10.2$ μm, respectively. The blue (red) dot denotes component 1 (component 2). (b) Imaginary part of the propagation constants (k_z) as a function of the Bloch momentum. (c) The Bloch mode corresponding to component 1 as $k_x = 0$. (d) The Bloch mode corresponding to component 2 as $k_x = \pi/d$. The positions of graphene sheets are denoted by the red dashed lines.

As the self-focusing nonlinearity of graphene would balance the normal diffraction [12], the two components of the vector solitons, respectively, arise from the Brillouin center $k_x = 0$ for $\lambda_1 = 9.8$ μm and the Brillouin edge $k_x = \pi/d$ for $\lambda_2 = 10.2$ μm, as presented with blue and red dots in Fig. 2(a). The real parts of the propagation constants are $\mathrm{Re}(k_z) = 49.1$ μm^{-1} and 39.7 μm^{-1}, respectively. The corresponding SPP wavelength for the two components are $\lambda_p = 0.13$ and 0.16 μm. The relation between the imaginary part of the propagation constant and the Bloch momentum is shown in Fig. 2(b), which reveals the propagation loss of the two components. The calculated propagation lengths of SPPs are given by $L_p = 6\lambda_p$ and $5\lambda_p$. The mode profiles for the two components without considering the nonlinearity are shown in Figs. 2(c) and 2(d), respectively. In each unit graphene pair of the GPA, the mode is formed by either symmetric or asymmetric coupling of SPPs in individual graphene. The profile corresponding to the first component ($k_x = 0$) is unstaggered at the neighboring periodic units, while the other one is staggered for the second component ($k_x = \pi/d$).

The dispersion relation also can be achieved by using a numerical computation [28]. The method is based on solving an eigenvalue equation based on Maxwell's equations, which is given by [8]

$$\begin{pmatrix} 0 & \frac{k_0\epsilon_r(x)}{\eta_0} \\ \frac{\eta_0}{k_0}\frac{\partial}{\partial x}\frac{1}{\epsilon_r(x)}\frac{\partial}{\partial x} + k_0\eta_0 & 0 \end{pmatrix} \begin{pmatrix} H_y \\ E_x \end{pmatrix} = k_z \begin{pmatrix} H_y \\ E_x \end{pmatrix}, \tag{2}$$

where $\epsilon_r(x)$ stand for the relative permittivity along the x axis. The transverse magnetic field and electric field, H_y and E_x, compose the eigenvector, while the propagation constant k_z is the eigenvalue. In the calculation, graphene is treated as a thin film with an equivalent thickness $\Delta \approx 1$ nm. Then, the relative equivalent permittivity of graphene could be given by $\epsilon_g = 1 + i\sigma_g\eta_0/(k_0\Delta)$ [29]. In the linear case, the calculated wave vectors of SPPs are given by $k_z = 50.05 + 0.65i$ μm^{-1} at $\lambda_1 = 9.8$ μm and $k_z = 40.52 + 0.68i$ μm^{-1} at $\lambda_2 = 10.2$ μm. The values coincide fairly with the exact results by solving Eq. (1). The method developed here aims at dealing with nonlinear systems.

Taking into account the nonlinearity, the surface conductivity of graphene can be written as $\sigma_g = \sigma_{g,\mathrm{linear}} + \sigma^{\mathrm{NL}}(|E_{z1}|^2 + |E_{z2}|^2)$. The nonlinear conductivity σ^{NL} is given by [19,20]

$$\sigma^{\mathrm{NL}} = -i\frac{3}{8}\frac{e^2}{\pi\hbar^2}\left(\frac{eV_F}{\mu_c\omega}\right)^2\frac{\mu_c}{\omega}, \tag{3}$$

where ω denotes the frequency and the Fermi velocity $V_F \approx c/300$. It is obvious that the equivalent permittivity of graphene is intensity-dependent. Considering the nonlinearity of graphene, Eq. (2) turns into a nonlinear eigenproblem, which could be solved by using the self-consistent method [30]. Two localized fields each having a Gaussian distribution are adopted as initial values for the iterative calculation. We set 80 V^2/μm^2 as the maximum intensity of the first component and 100 V^2/μm^2 for the second. In each step of the iteration, the permittivity of graphene is updated with the solved field distribution of the previous step. Repeating the process of solving the field distribution of the two components and updating the permittivity, we can obtain the transverse distribution of the vector PLSs until the eigenvalues are stable. The results are shown in Fig. 3. From Fig. 3(a), the first component ($\lambda_1 = 9.8$ μm) has a similar but localized profile in
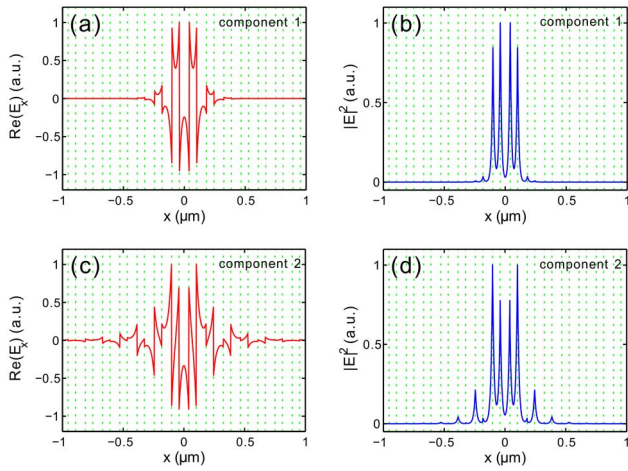
Fig. 3. For the first component of the vector PLSs arising from the Brillouin center $k_x = 0$ for $\lambda_1 = 9.8$ μm; (a), (b) normalized transverse electric field (E_x) and intensity distribution. For the second component arising from the Brillouin edge $k_x = \pi/d$ for $\lambda_2 = 10.2$ μm; (c), (d) normalized transverse electric field (E_x) and intensity distribution. Positions of graphene sheets are denoted by the green dashed lines.

Fig. 4. (a), (b) Stable propagation of the first component and the second component without loss. (c), (d) Single propagation of the first component and the second component when the other one is removed. (e), (f) Stable propagation of the first component and the second component in lossy GPAs. The field distribution is shown by $\log(|E|^2)$ in all figures.

comparison with the Bloch mode shown in Fig. 2(c). It could be viewed as nonlinear counterpart of the Bloch mode in the Brillouin center of the first band. The intensity distribution of the first component, $|E|^2 = |E_x|^2 + |E_z|^2$, is illustrated in Fig. 3(b). The FWHM of the first component is about 0.22 μm or $0.02\lambda_1$. The sharp peaks of the intensity reveal the strong confinement of SPPs on the graphene sheets. The transverse electric field and the intensity of the second component are shown in Figs. 3(c) and 3(d). The effective width of the vector PLSs for the two components is given by [9,10]

$$w_{1,2} = \left(\int x^2 |E_{1,2}|^2 dx / \int |E_{1,2}|^2 dx \right)^{1/2}. \qquad (4)$$

The calculated results are $w_1 = 0.08$ μm and $w_2 = 0.13$ μm, corresponding to $0.008\lambda_1$ and $0.013\lambda_2$, respectively. Because the band curve of the second component has a larger curvature than that of the first component, it has a little bit larger width.

To shed more light on vector PLS, we also investigate their propagation by using the modified split-step Fourier beam propagation method [8]. The propagation of vector PLS without considering the loss of graphene is shown in Figs. 4(a) and 4(b). It shows that the two components of the vector soliton remain constant lateral profiles all the time during propagation. If one of the two components is absent, the other has to suffer remarkable diffraction, as shown in Figs. 4(c) and 4(d). A stationary propagation of vector PLS requires both components at work. In other words, the two components influence each other simultaneously. The propagation of one component can be controlled by the other one. Taking the loss into consideration, the propagation of the vector PLS is illustrated in Figs. 4(e) and 4(f). The propagation distances of both components are roughly the same. The propagation distance of the second component is a little bit smaller than that of the first one because the loss rests with the original linear eigenmodes, as shown in Fig. 2(b). The propagation loss of the first component is smaller than the second one. Thereafter, the propagation length of the vector PLSs is mainly determined by the second component.
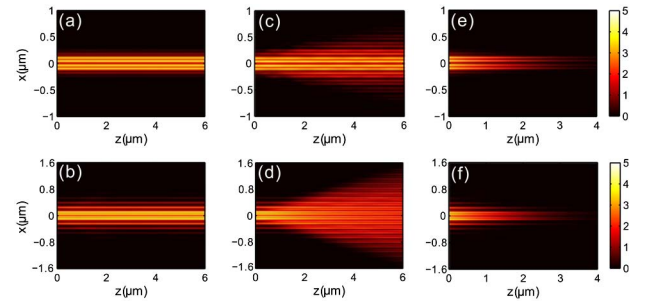
The propagation constants of the two components versus the peak intensity of the second component denoted by I_2 are plotted in Figs. 5(a) and 5(b). One sees that the propagation constants of both components increase as I_2 increases. For a fixed value of I_2, the propagation constants also increase as the peak intensity of the first component I_1 increases. Considering that the second component, originating from the second band, is located in the bandgap, the intensity I_2 should reach the maximum at the bottom of the first band for each value of I_1. The limitation of I_2 also appears for the first component as I_1 varies, although the first component originates from the first band and lies in the semi-infinite gap above, as shown in Fig. 5(a). When the intensity $I_1 = 0$ or $I_2 = 0$, the vector PLSs turn to scalar solitons. It should be mentioned that there is a bound state for the first (second) component even if its intensity approaches to zero, which results from the nonlinear mutual self-trapping effect induced by the second (first) component.

The influence of I_2 on the effective width is shown in Figs. 5(c) and 5(d). The effective width of the first component
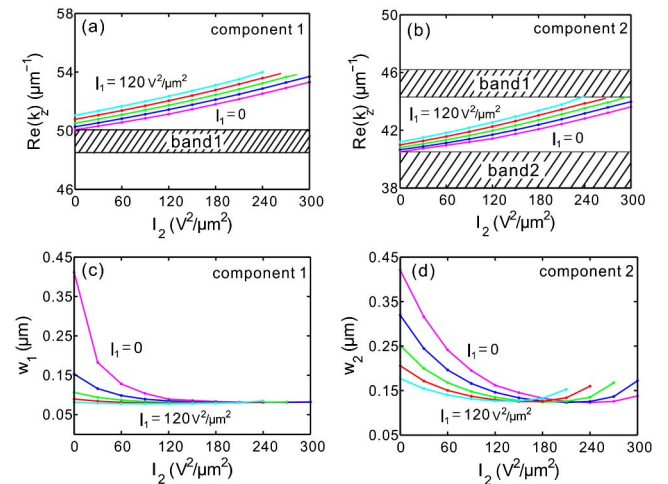
Fig. 5. (a), (b) Propagation constants of the first component and the second component vary with the intensities of both components. $I_1 = 0$, 30, 60, 90, 120 $V^2/\mu m^2$. (c), (d) Effective width of the first component and the second component vary with the intensities of both components.
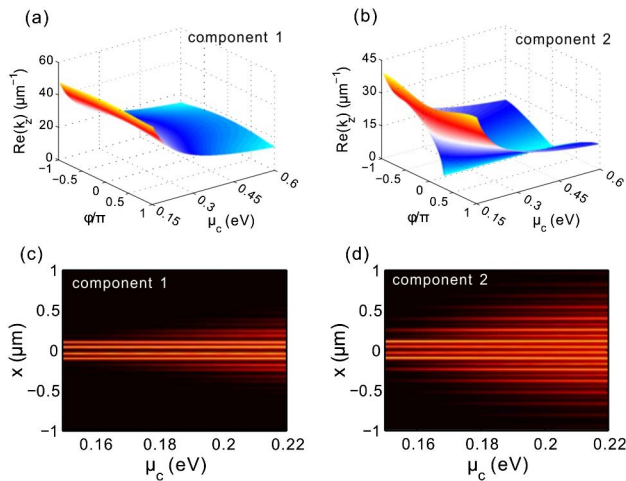
Fig. 6. (a) For the first component $\lambda_1 = 9.8$ μm, the first band varies with the chemical potential of graphene. (b) For the second component $\lambda_2 = 10.2$ μm, the second band varies with the chemical potential of graphene. (c), (d) Transverse distributions of the first component and the second component vary with the chemical potential.

decreases as the intensities I_1 and I_2 increase. When $I_1 > 60$ V^2/μm^2 or $I_2 > 120$ V^2/μm^2, the value of w_1 almost keeps at constant, as shown in Fig. 5(c). In this circumstance, the first component has concentrated into the region of a single graphene pair with a width about 0.06 μm and can no longer be squeezed. As for the second component shown in Fig. 5(d), the effective width decreases first, and then increases after reaching a minimum of $w_2 = 0.12$ μm. The minimum is almost independent on I_1. The width of the second component reaches its minimum as its propagation constant locates in the middle of the bandgap. As I_2 increases further, the propagation constant approaches to the bottom of the first band and the width increases.

We also investigate the influence of chemical potential. The variation of band structure with chemical potential for the linear case is shown in Figs. 6(a) and 6(b). Here we only provide the first (second) band for the first (second) component as $\lambda_1 = 9.8$ μm ($\lambda_2 = 10.2$ μm). Generally, the propagation constants corresponding to different components decrease as the chemical potential increases. From Fig. 6(a), the curvature at the Brillouin center increases as the chemical potential increases, where the first component is growing. As a result, the first component becomes wider as the chemical potential increases, as shown in Fig. 6(c). The situation is roughly the same for the second component but for a larger beam width, as shown in Figs. 6(b) and 6(d). The reason lies in the fact that the curvature of the second band is remarkably larger than the first one, indicating stronger diffraction of SPPs. It should be noted that the maximum intensities of two components are fixed at $I_1 = 80$ V^2/μm^2 and $I_2 = 100$ V^2/μm^2, respectively. By comparing the variation of two components, the second one is more sensitive to the chemical potential than the first one in the range of $\mu_c = 0.15$–0.22 eV. As the chemical potential increases further, strong coupling occurs, and the case is out of our consideration scope, as shown in Fig. 6(b).

In conclusion, we have investigated the vector PLSs in nonlinear graphene-pair arrays. Every graphene pair of GPAs consisting of two separated parallel graphene sheets can support symmetric and antisymmetric SPP modes. Consequently, there should be two bands of SPP Bloch modes in GPAs. The components of the vector solitons have different frequencies and arise from Bloch modes of two bands in GPAs. They undergo mutual self-trapping through the balance between SPPs diffraction and the nonlinearity effect of graphene. Due to the strong confinement of SPPs in graphene, the vector PLSs manifest a deep-subwavelength width. By varying the chemical potential of graphene, the effective width of vector PLSs can be flexibly tuned. This study may find applications in optical switches, optical circuits, and soliton-based navigation on a deep-subwavelength scale.

REFERENCES

1. V. E. Zakharov and A. B. Shabat, Sov. Phys. J. Exp. Theor. Phys. **34**, 62 (1972).
2. H. Eisenberg, Y. Silberberg, R. Morandotti, A. R. Boyd, and J. S. Aitchison, Phys. Rev. Lett. **81**, 3383 (1998).
3. G. I. Stegeman and M. Segev, Science **286**, 1518 (1999).
4. Z. Chen, A. Bezryadina, and I. Makasyuk, Opt. Lett. **29**, 1656 (2004).
5. J. Meier, J. Hudock, D. Christodoulides, G. Stegeman, Y. Silberberg, R. Morandotti, and J. S. Aitchison, Phys. Rev. Lett. **91**, 143907 (2003).
6. D. N. Christodoulides and R. I. Joseph, Opt. Lett. **13**, 794 (1988).
7. Y. S. Kivshar, Opt. Lett. **18**, 1147 (1993).
8. Y. Liu, G. Bartal, D. A. Genov, and X. Zhang, Phys. Rev. Lett. **99**, 153901 (2007).
9. Y. Kou, F. Ye, and X. Chen, Opt. Lett. **38**, 1271 (2013).
10. O. Cohen, T. Schwartz, J. W. Fleischer, M. Segev, and D. N. Christodoulides, Phys. Rev. Lett. **91**, 113901 (2003).
11. Y. Xue, F. Ye, D. Mihalache, N. C. Panoiu, and X. Chen, Laser Photon. Rev. **8**, L52 (2014).
12. H. Eisenberg, Y. Silberberg, R. Morandotti, and J. S. Aitchison, Phys. Rev. Lett. **85**, 1863 (2000).
13. A. V. Zayats and I. I. Smolyaninov, J. Opt. A **5**, S16 (2003).
14. W. L. Barnes, A. Dereux, and T. W. Ebbesen, Nature **424**, 824 (2003).
15. B. Wang, X. Zhang, F. J. García-Vidal, X. Yuan, and J. Teng, Phys. Rev. Lett. **109**, 073901 (2012).
16. H. Huang, B. Wang, K. Wang, H. Long, and P. Lu, Opt. Lett. **39**, 5957 (2014).
17. F. J. García de Abajo, ACS Photonics **1**, 135 (2014).
18. A. Vakil and N. Engheta, Science **332**, 1291 (2011).
19. S. A. Mikhailov and K. Ziegler, J. Phys. **20**, 384204 (2008).
20. D. A. Smirnova, I. V. Shadrivov, A. I. Smirnov, and Y. S. Kivshar, Laser Photon. Rev. **8**, 291 (2014).
21. H. Deng, F. Ye, B. A. Malomed, X. Chen, and N. C. Panoiu, Phys. Rev. B **91**, 201402(R) (2015).
22. M. Conforti, C. D. Angelis, T. R. Akylas, and A. B. Aceves, Phys. Rev. B **85**, 063836 (2012).
23. B. Wang, X. Zhang, X. Yuan, and J. Teng, Appl. Phys. Lett. **101**, 13111 (2012).
24. A. Auditore, C. Angelis, A. Locatelli, and A. B. Aceves, Opt. Lett. **38**, 4228 (2013).
25. N. M. R. Peres, Rev. Mod. Phys. **82**, 2673 (2010).
26. S. Ke, B. Wang, H. Huang, H. Long, K. Wang, and P. Lu, Opt. Express **23**, 8888 (2015).
27. F. Wang, C. Qin, B. Wang, S. Ke, H. Long, K. Wang, and P. Lu, Opt. Express **23**, 31136 (2015).
28. Z. Wang, B. Wang, H. Long, K. Wang, and P. Lu, Opt. Express **23**, 32679 (2015).
29. M. L. Nesterov, J. Bravo-Abad, A. Y. Nikitin, F. J. Garcia-Vidal, and L. Martin-Moreno, Laser Photon. Rev. **7**, L7 (2013).
30. M. Mitchell, M. Segev, T. H. Coskun, and D. N. Christodoulides, Phys. Rev. Lett. **79**, 4990 (1997).